npj | Climate and Atmospheric Science

www.nature.com/npjclimatsci

ARTICLE OPEN

Check for updates

Global-scale constraints on light-absorbing anthropogenic iron oxide aerosols

K. D. Lamb[1,2✉], H. Matsui[3], J. M. Katich[1,2], A. E. Perring[1,2], J. R. Spackman[4], B. Weinzierl[5], M. Dollner[5] and J. P. Schwarz[2]

Anthropogenic iron oxide aerosols (FeO_x) have been identified as a climatically significant atmospheric light absorber, and as a contributor of free iron to the oceans. Here we provide global-scale constraints on their atmospheric abundance with measurements over the remote Pacific and Atlantic Oceans from aircraft campaigns spanning 10 years. We find FeO_x-like aerosols are transported far from source regions with similar efficiency as black carbon particles. Strong contrast in concentrations was observed between the Northern and Southern Hemisphere Pacific. We provide observational constraints in remote regions on the ambient ratios of FeO_x relative to BC from fossil fuel burning. Comparison with a global aerosol model tuned to recent observations in East-Asian source regions confirm an upward revision of emissions based on model/observation comparison over the Pacific receptor region. We find that anthropogenic FeO_x-like particles generate global-scale shortwave atmospheric heating 0.3–26% of that of black carbon in remote regions where concentrations of both aerosols are very low.

npj Climate and Atmospheric Science (2021)4:15 ; https://doi.org/10.1038/s41612-021-00171-0

INTRODUCTION

Light-absorbing aerosols such as black carbon (BC), brown carbon (BrC), and mineral dust play an important role in the atmosphere due to their significant contribution to shortwave atmospheric heating[1]. Recent in situ measurements with a single particle soot photometer (SP2) over East Asia during the Aerosol Radiative Forcing in East Asia (A-FORCE) aircraft campaign identified iron oxide aerosols (FeO_x) associated with anthropogenic processes as an overlooked source of atmospheric absorption, contributing 4–7% of that attributed to BC in the shortwave[2]. Similar results in the region have been confirmed by ground-based studies[3], linking FeO_x observed by the SP2 in East Asia to anthropogenic combustion sources[4].

A global modeling study based on observations of FeO_x in continental Asian outflow during A-FORCE and ground-based observations of European outflow found anthropogenic combustion iron emissions could be underestimated by as much as 5 times on a global scale[5]. Pyrogenic iron oxides from combustion sources have been estimated to have a direct radiative effect of 0.4–1.0 W m^{-2} over East Asia, ~10% of the radiative effect attributed to BC[6]. These past studies have been limited to observations of regional loadings near significant anthropogenic source regions in the Northern Hemisphere. Here we investigate the global-scale contribution of FeO_x to direct climate effects with near pole-to-pole latitude range observations over the remote oceans.

Our remote observations also have important implications for understanding the iron biogeochemical cycle, as combustion aerosols may be an important source of particulate free iron for the oceans[5–7]. Although the total iron emissions associated with combustion aerosols is significantly lower than the iron emissions associated with mineral dust sources, iron in combustion aerosols may be much more soluble, leveraging combustion's overall importance for iron bioavailability relative to dust in certain regions[8]. Comparisons between four global models and multiple field observations have recently linked observations of high aerosol Fe solubility to atmospheric processing of pyrogenic iron oxides[9]. Combustion iron aerosols may be particularly important in the Southern Hemisphere, as particulate Fe deposition to the high-nutrient, low-chlorophyll zones (where there is direct correlation between atmospheric iron inputs and phytoplankton abundance) in the Southern Oceans could impact marine primary productivity[8].

A recent review of iron aerosol deposition to the oceans indicated that the role of anthropogenic combustion aerosols is particularly challenging to constrain due to their low concentrations and a lack of reliable atmospheric observations[10]. If global emissions of FeO_x aerosols from anthropogenic sources have a similar ratio to BC emissions as reported in East Asia[2], these aerosols would provide 52% higher particulate iron deposition to the Southern Oceans than previously estimated[5]. Low isotope ratios in Fe-containing aerosols associated with anthropogenic combustion[11] and in North Atlantic and Pacific marine aerosol samples[12,13] have provided additional evidence that anthropogenic aerosols contribute bioavailable iron to the oceans[14–16]. These results could have important consequences for the uptake of CO_2 emissions by the oceans, and they suggest anthropogenic combustion iron aerosol emissions play a more significant role in climate than previously believed. However, the lack of observations in the Southern Hemisphere is a significant source of uncertainty[5,9].

All of these recent results have indicated even very low concentrations of anthropogenic combustion iron oxide aerosols could have important impacts on climate. Such low concentrations pose a significant challenge for aircraft observations in remote regions, however. To address this challenge and provide extended observational constraints of FeO_x on a global scale, we have extracted FeO_x information from a large number of observations from aircraft campaigns sampling over the remote Pacific and Atlantic, consisting of ~730 total flight hours. We

[1]Cooperative Institute for Research in the Environmental Sciences, University of Colorado, Boulder, CO, USA. [2]Chemical Sciences Division, NOAA Earth System Research Laboratory, Boulder, CO, USA. [3]Graduate School of Environmental Studies, Nagoya University, Nagoya, Japan. [4]NASA Ames Research Center, Mountain View, CA, USA. [5]Faculty of Physics, Aerosol Physics and Environmental Physics, University of Vienna, Vienna, Austria. ✉email: kara.lamb@colorado.edu

Published in partnership with CECCR at King Abdulaziz University

npj nature partner journals

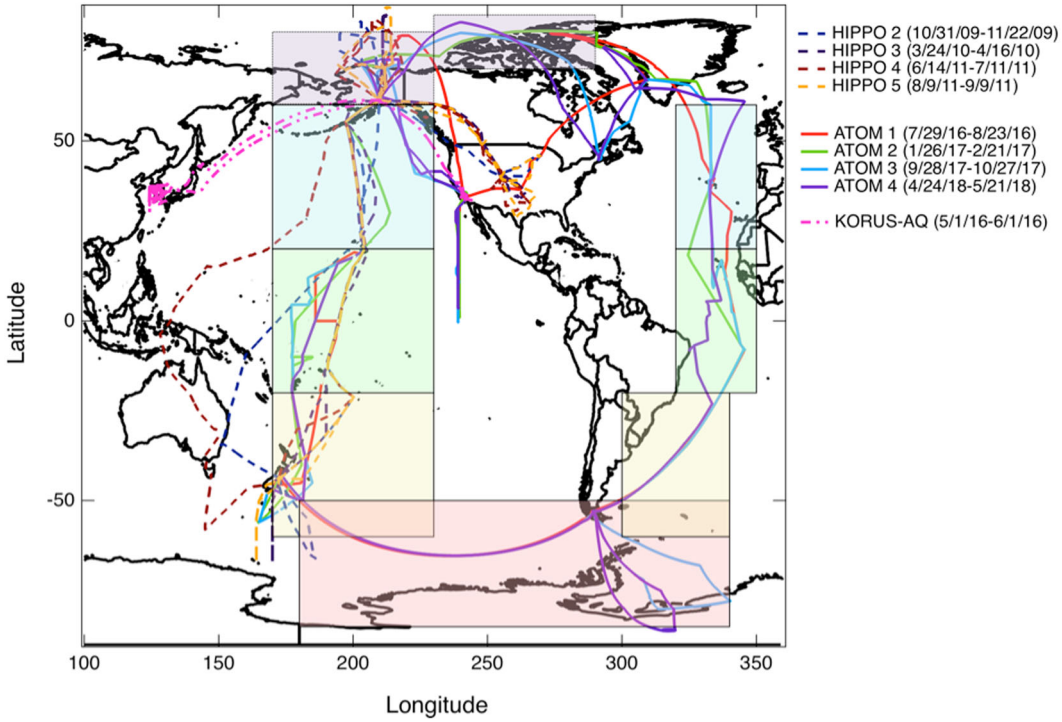

Fig. 1 Flight paths of the research aircraft for the HIPPO, KORUS-AQ, and ATom campaigns. Observations from research flights spanning four seasons and 9 years are used in this analysis. The shaded boxes show boxes used in the calculation of average regional values given in Table 1 and vertical profiles (purple—60°N–80°N for Pacific and 70°N–85°N for Atlantic, blue—20°N–60°N, green—20°S–20°N, yellow—60°S–20°S, red—Southern Ocean) shown in Figs 6, 7.

present this dataset of in situ airborne measurements of light-absorbing metallic (LAM) aerosols in cloud-free regions measured by the NOAA SP2 during the High-performance Instrumented Airborne Platform for Environmental Research (HIAPER) Pole-to-Pole Observations (HIPPO) research campaigns in 2009–2011[17], and the 2016–2018 Atmospheric Tomography Mission (ATom)[18]. These observations cover eight measurement periods over the remote Pacific and four measurement periods over the remote Atlantic. They contain observations from 86°S to 86°N, including over-flights of the Arctic and Antarctic, and altitudes from near the surface to nearly 14 km. We also use near-source observations during the Korean United States Air Quality Study (KORUS-AQ) to characterize the NOAA SP2 response to populations of aerosols associated with anthropogenic pollution in source regions, demonstrating light-absorbing FeO_x similar to that observed over continental East Asia and associated with anthropogenic sources is present in the remote background. Figure 1 shows the flight paths for all measurement series. We compare these observations with results from a global aerosol model incorporating anthropogenic magnetite emissions consistent with recent atmospheric observations in source regions[5]. In the remote receptor region influenced by East-Asian outflow, the observations confirm the revised emission estimates for anthropogenic magnetite in Matsui et al.[5]. The observations over the global scale provide constraints on FeO_x shortwave atmospheric heating relative to BC.

RESULTS

In situ observations of LAM aerosols

The observations discussed here were made with a NOAA Single Particle Soot Photometer (SP2), which detects individual light-absorbing refractory aerosol particles such as BC via laser-induced incandescence (LII). The SP2 provides real time in situ quantification of refractory aerosol mass and number density[19]. Following the established literature (e.g.,[20]) we denote the BC material specifically quantified with the SP2 as "refractory black carbon" (rBC). Single aerosol particles containing metallic components, which are also measured by the SP2, are distinguishable from rBC by differences in their characteristic evaporation temperatures[21].

To quantify FeO_x concentrations over the remote oceans, we first differentiate metallic aerosols from rBC (Supplementary Fig. 1) based on their SP2 color-temperature ratio (which depends on evaporation temperature) and incandescent peak amplitude (which depends on refractory particle mass), and designate these aerosols as LAM aerosols. We report observations of rBC and LAM particles in the volume equivalent diameter ranges of 100–500 nm for rBC (assuming a void-free density of 1.8 g cm^{-3}) and 180–1290 nm for LAM (assuming that LAM detectable by LII is predominantly FeO_x, with a void-free density of 5.17 g cm^{-3}).

LAM aerosols observable with the SP2 may include aerosols from both natural sources (mineral dust or volcanic ash) or from anthropogenic combustion sources[21,22]. Aerosols with metallic components from natural sources are detected with low efficiency in smaller sizes, while the SP2 has previously been shown to detect pure iron oxide laboratory samples (e.g., magnetite and hematite used as a proxy for anthropogenic combustion iron oxides) with high efficiency over much of its size range[21], with ~100% of magnetite mass detected in this size range (Supplementary Fig. 7). Anthropogenic iron oxides as identified here are likely comprised of a wider class of materials than pure magnetite or hematite[23].

To characterize the portion of LAM aerosols observed by the SP2 and attributable to anthropogenic combustion iron oxides, we further differentiate LAM aerosols based on their single particle optical properties (see "Methods" and Supplementary Methods for details). This allows classification of individual particles, via their characteristic behavior in the SP2, as either anthropogenically-sourced or naturally-generated.

Three distinct subpopulations of LAM aerosols were detected by the SP2 in both East Asia during KORUS-AQ and over the remote

Table 1. Characteristics of LAM observed in cloud-free regions with an SP2.

Region	LAM/rBC (number)	LAM/ rBC (mass)	# FeO_x-like (number)	# Dust-like (number)	# Artifact-like (number)	FeO_x-like: LAM (number)	FeO_x-like: LAM (mass)
Pacific (60°N–80°N)	0.0022	0.20	400	252	56	0.61	0.47
Pacific (20°N–60°N)	0.0015	0.18	1457	984	109	0.60	0.51
Pacific (20°S–20°N)	0.0017	0.47	413	371	30	0.53	0.52
Pacific (60°S–20°S)	0.0006	0.15	363	276	68	0.57	0.45
Atlantic (70°N–85°N)	0.0014	0.13	221	96	14	0.70	0.55
Atlantic (20°N–60°N)	0.0018	0.22	587	603	31	0.49	0.52
Atlantic (20°S–20°N)	0.0007	0.51	1268	3441	124	0.27	0.23
Atlantic (60°S–20°S)	0.0004	0.13	47	25	3	0.65	0.70
Southern Ocean	0.0006	0.13	223	127	16	0.64	0.69
East Asia	0.0040	0.19	49,387	16,409	2628	0.75	0.46

Remote regions are defined as shown in Fig. 1. The Atlantic observations are from the ATom campaigns only. Values from East Asia (from observations during the KORUS-AQ campaign) are given for comparison to a polluted source region. The ratio of LAM to rBC by number concentration and by mass concentration is given in columns 1 and 2, respectively. The total number of LAM particles observed in each region is given in columns 3–5. The last two columns provide the ratio of anthropogenic FeO_x to total LAM particles observed in that region by both number and total mass. Note that the Southern Ocean region overlaps with Southern Hemisphere Pacific and Atlantic regions.

Atlantic and Pacific Oceans during ATom and HIPPO. These three populations (anthropogenic FeO_x, dust-like particles, and artifact particles) were distinguished via their characteristic behavior in the SP2. The artifacts were associated with in-cloud measurement periods where particles generated from inlet shattering by ice crystals have been shown to be significant. As the artifacts are not representative of actual ambient aerosols, we exclude these particles from our analysis, and the total LAM reported here is split between anthropogenically-sourced FeO_x-like aerosols and naturally-generated dust-like populations. SP2 response to mineral dust from different source regions has not been fully characterized, and the majority of metallic oxides in mineral dust may be contained in coarse mode aerosols beyond our detection limit; hence we interpret concentrations of dust-like LAM aerosols only in a relative sense here.

The majority of LAM aerosols observed in East Asia in previous work was associated with anthropogenic pollution using independent filter-based measurements and source apportionment methods[2–4], and the most significant population of LAM aerosols observed during KORUS-AQ over East Asia belonged to the anthropogenic FeO_x-like population (see Table 1). Vertical profiles of FeO_x mass loadings during KORUS-AQ were consistent with those previously observed during the A-FORCE campaign in East Asia (Supplementary Fig. 10)[2].

Observations of LAM and rBC over the remote oceans

Figure 2 summarizes the LAM concentrations in ng (std. m)$^{-3}$ binned by latitude (1° bins) and altitude (0.5 km bins) over the Pacific and Atlantic Oceans, while Fig. 3 shows the relative fraction of anthropogenic FeO_x-like aerosols to total LAM aerosol mass observed in each bin. HIPPO and ATom observations reflect a comprehensive picture of the global distribution of these aerosols in remote regions, with extensive vertical profiling from the surface to ~8 km (HIPPO) and ~12 km during (ATom), with some data up to ~14 km altitude.

A major challenge of in situ LAM observations in remote regions is the low concentrations relative to sampling time. Because the SP2 detects aerosols on a single particle basis, total mass concentration is determined by integrating observed single particle masses and dividing by total sampling volume. Data sets from HIPPO 2–5 and ATom 1–4 were merged to reduce statistical uncertainties in remote regions with low concentrations of LAM. These observations cover the periods from 2009 to 2011 (HIPPO) and 2016 to 2018 (ATom), and include data from every season (see "Methods" for campaign details). For the Pacific, each spatial bin includes, on average, 380 s of sampling time, while bins in the Atlantic represent an average of 140 s (because the HIPPO dataset did not contribute to observations over the Atlantic). In general,

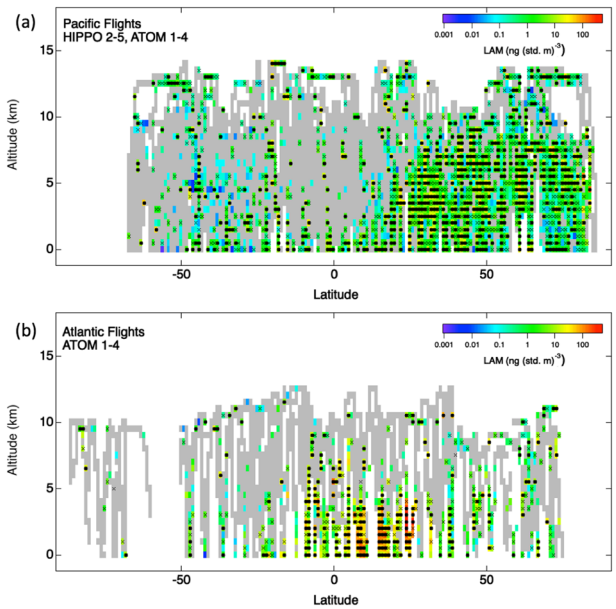

Fig. 2 Global distributions of LAM aerosols over remote Pacific and remote Atlantic. Observations of average LAM concentrations (ng (std. m)$^{-3}$) in cloud-free regions, with data gridded to a resolution of 0.5 km vertical and 1° latitude. Pacific (Panel **a**) is defined as observations in the longitude band from 150° to 225°. Atlantic (Panel **b**) are observations in the longitude band from 300° to 350°. Gray indicates we sampled air, but that the average concentration of LAM was <0.001 ng (std. m)$^{-3}$, while white indicates no data. Solid black dots indicate that observations satisfy the strong sampling criteria, while black crosses indicate observations satisfy the weak sampling criteria (see "Methods"). Measurements over the Pacific include observations from eight aircraft campaigns (HIPPO 2–5 and ATom 1–4), while measurements over the Atlantic include observations from four aircraft campaigns (ATom 1–4).

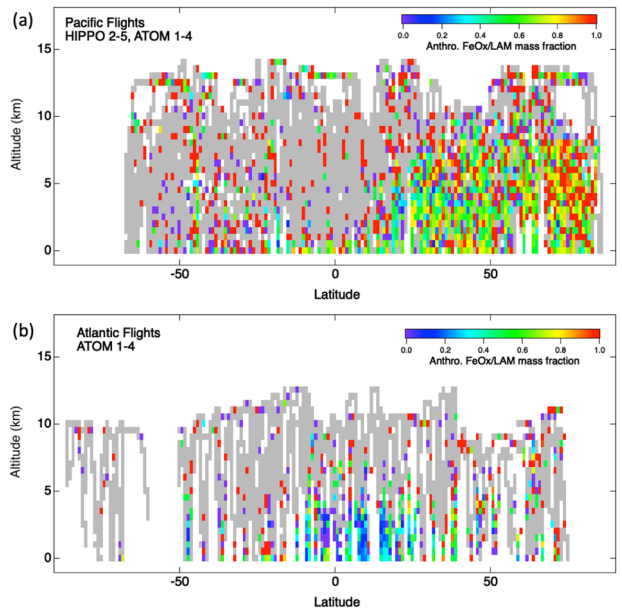

Fig. 3 Relative anthropogenic-like FeO_x to total LAM aerosol mass over remote Pacific and Atlantic. Each bin represents a 0.5 km by 1.0° latitude over the Pacific (Panel **a**) and Atlantic (Panel **b**). Observations are only shown in cloud-free regions where LAM aerosols were detected by the SP2.

wide swaths of the remote atmosphere are exceptionally clean of LAM, especially in the Southern Hemisphere and in the free troposphere. Because LAM number concentration was typically ~3 orders of magnitude lower than that of rBC in most regions (see Table 1, column 1), even these long sampling times were insufficient to drive statistical uncertainties to negligible levels. A Monte Carlo simulation (similar to[24]) was performed to evaluate whether the observed concentrations (in ng/std. m^3) of LAM in each bin represented a statistically significant sampling. Figure 2 identifies the bins that exceed a "strong sampling criterion" with high confidence in the concentrations (black dot markings); bins with "weak sampling criterion" with poorer confidence in the concentration (cross markings); and grayed out bins with <0.001 ng (std. m)$^{-3}$ concentration. The Methods section explains these calculations, defines the strong and weak criteria, and points to further discussion in Supplementary Methods.

Although our observations indicate that LAM was not as common as rBC on a global-scale, individual LAM particles are more massive than individual rBC. Hence the ratio of observed mass concentrations indicated that LAM mass concentrations can be a significant fraction of rBC in the Northern Hemisphere Pacific, and from the Southern subtropics to the Atlantic midlatitudes (Supplementary Fig. 13). A large-scale summary of the LAM in each region is provided in Table 1, to provide context about approximate statistics in number and mass space in different regions. In the observable size range of the modified SP2, the LAM mass was 0.13–0.51 the rBC mass, with the highest ratios observed in the Atlantic (between 20°S and 20°N) and the lowest ratios observed in the southern Atlantic and Southern Oceans (Table 1, column 2). In each of these regions, anthropogenic FeO_x-like aerosols were a significant portion of the total observed LAM mass (23–70%). Anthropogenic FeO_x was detected in all altitudes for every region, even as it formed a different fraction of total LAM (Fig. 3).

The contrast in LAM mass loadings between the Northern and Southern Hemispheres was pronounced (Fig. 2). In much of the Southern Hemisphere (with the exception of the enhanced concentrations in the subtropics near 20°S), the mass loadings of LAM were below detectable limits (Supplementary Fig. 12). Compared to rBC (Supplementary Fig. 14), LAM demonstrated stronger contrast between the Northern and Southern Hemispheres. Both species had very low concentrations at higher altitudes in the equatorial regions of the Pacific and Atlantic, a feature previously observed for rBC and associated with the injection of clean air via convection being balanced by extra-tropical mixing into the tropical tropopause layer[24,25].

Figure 2a also shows that relatively high atmospheric loadings of LAM were present over the Northern Hemisphere Pacific (20°N to 60°N and 60°N to 80°N), and in the tropics over the Atlantic. Arctic loadings were very consistent with those in the lower Northern latitudes, likely due to the lack of significant local sources, long lifetimes, and thorough vertical mixing with long-range transport.

Statistics for LAM in the midlatitudes Pacific (20°N to 60°N) were sufficient for evaluation of LAM's seasonal dependence in the region (Fig. 4a). The similar seasonal trend for the observed mass loadings of LAM and rBC was consistent with influences from anthropogenic pollution sources. The highest loadings were observed during the HIPPO 3 campaign, which took place in the spring of 2010 (March 24–April 16, 2010), when the strongest influence of continental Asian outflow over the northern Pacific was observed[24,26]. ATom 4 (April 24–May 21, 2018) similarly measured enhanced LAM mass loadings, consistent with enhanced Asian outflow in the spring. An analysis of trans-Pacific transport of BC during HIPPO 3 using inverse modeling indicated nearly 90% of rBC over the central Pacific in latitudes with strong Asian influences was associated with fossil fuel and biofuel combustion[26]. Hence, the ratio of LAM to rBC further indicates similar source contributions. Specifically, the LAM concentrations shown in Fig. 4a, vary widely, with an approximate standard deviation of ~an order of magnitude. Yet, the ratio of LAM to rBC (Fig. 4b) varies with only an approximate standard deviation of factor of three. This suggests that rBC and LAM co-vary significantly in the remote in this region.

The mass fraction of LAM associated with anthropogenic FeO_x-like aerosols in the N. Pacific (47–51%) was also consistent with the observations over East Asia (46%). The observed seasonal trend further agreed with the modeling results in[5], which found greater agreement with observations of total iron concentrations in Asian outflow measured at a ground site in Gosan when including higher emission estimates from anthropogenic combustion iron[27].

Over the Atlantic, observations between 5°S and 30°N indicated the highest concentrations of LAM were in the Saharan Air Layer (SAL), generally at altitudes below 5 km (Fig. 2b). This region of high LAM concentrations overlapped with the significant influence of biomass burning (BB) from wildfires in Western Africa[28], although the region strongly influenced by BB extended further south, over 20°S to 30°N. LAM observed by the SP2 in the SAL demonstrated significantly greater variance in SP2 color ratio than LAM observed over the northern Pacific, likely due to greater variability in the types of metallic oxides present in natural mineral dust[21,22]. The SP2-responses for these aerosols indicated the majority of the observed mass was associated with dust-like LAM (Fig. 3b), with nearly 80% of LAM mass attributed to dust-like aerosols in this region, with the majority of these aerosols detected at altitudes below 5 km.

The dN/dLogD number distributions for all LAM aerosols averaged over the entire remote Pacific and remote Atlantic and associated with either anthropogenic combustion aerosols or with natural mineral dust are shown in Fig. 5a. In the Pacific, a greater number density of FeO_x-like aerosols at small sizes (with a mode peaking below the SP2 detection limit at ~200 nm volume equivalent diameter) was observed, similar to the dN/dLogD observed in East Asia during KORUS-AQ (Fig. 5b). These results were consistent with the observed size distributions in East-Asian

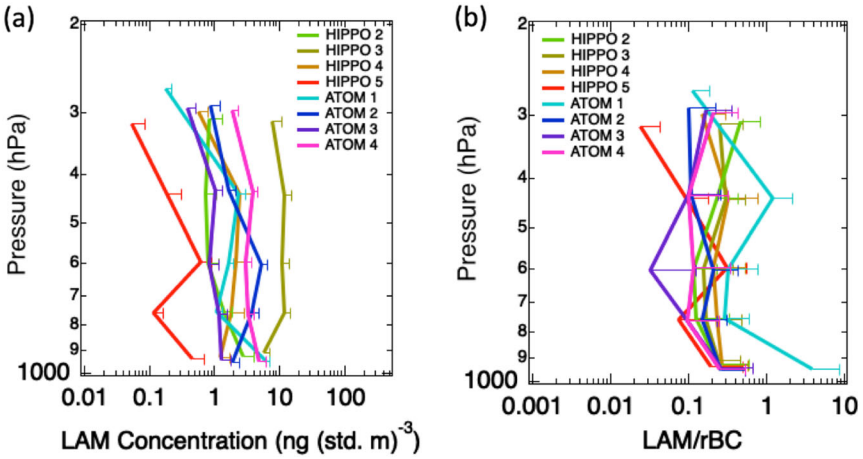

Fig. 4 Seasonality of LAM and LAM/rBC over the N. Hemisphere Pacific. Average vertical profiles for the remote Pacific between 20°N and 60°N for different seasons from the HIPPO and ATom campaigns are shown. LAM concentration (**a**) is given in ng (std. m)$^{-3}$. The total number of observed LAM vertical sampling periods included in the average vertical profile for each campaign is given in parentheses after the campaign name and observation period: HIPPO 2—Oct./Nov. 2009 (34); HIPPO 3—March/April 2010 (35); HIPPO 4—June/July 2011 (36); HIPPO 5—Aug./Sept. 2011 (35); ATom 1—July/Aug. 2016 (11); ATom 2—Jan./Feb. 2017 (31); ATom 3—Sept./Oct. 2017 (26); ATom 4—April/May 2018 (22). Observations are binned to 160 hPa, and error bars indicate 1 standard deviation and are only shown for the higher range (assuming observations in a single bin are normally distributed). To determine vertical profiles of the ratio of LAM/rBC from observations (**b**), average vertical profiles for LAM and rBC are calculated for each season and then divided to determine the ratio at each altitude level, as we assume that remote regions are well-mixed. Error bars for the ratio indicate 1 standard deviation and are determined by propagation of uncertainty, under the assumption that errors between observed LAM and rBC concentrations are uncorrelated.

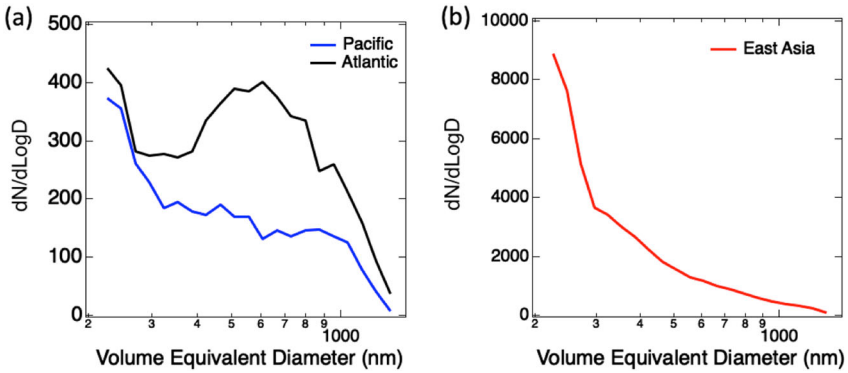

Fig. 5 Size distributions for LAM aerosols observed over Atlantic and Pacific and East Asia. The dN/dLogD size distributions for aerosols observed over the remote Pacific and remote Atlantic (**a**) and in East Asia (**b**) are shown as a function of the aerosols' volume equivalent diameter, assuming LAM aerosols have a void-free density of 5.17 g cm^{-3}. The SP2's detection range falls off below 250 nm and above 1000 nm. We exclude aerosols identified as artifacts.

outflow during the A-FORCE campaign, which found dN/dLogD peaking below 200 nm in the planetary boundary layer. This mode was linked with anthropogenic combustion iron sources, while an increasing fraction of LAM observed at higher altitudes during A-FORCE had larger volume equivalent diameters (VED) and were associated with dust[2].

The Atlantic dN/dLogD size distribution demonstrated evidence of a mode peaking below 200 nm, as well as a significant mode near 500 nm, which was consistent with the greater influence of dust-like aerosols in this region. Previously a modified SP2 has been used to investigate the hematite fraction in the Sahel-influenced dust SAL, which is known to have a higher fraction of hematite than other natural dust sources[29], and also observed dN/dLogD consistent with the mode near 500 nm for these aerosols. Indications of both anthropogenic and natural source contributions were also consistent with recent measurements of isotopic iron in bulk marine aerosols collected over the Atlantic in this region, which found evidence of both highly soluble anthropogenic Fe and poorly soluble Fe associated with dust in Saharan-dominated air samples[12]. Modeling results in[12] linked this soluble anthropogenic Fe with anthropogenic combustion sources, consistent with the smaller dN/dLogD size mode that we observed in the ATom Atlantic observations.

The dN/dLogD size distributions by region (Supplementary Fig. 15) over the remote oceans demonstrated either or both the combustion mode and hematite dust mode were present in every region. With the exception of the latitude band from 20°S to 20°N, aerosols observed over the Pacific were mainly associated with the smaller combustion mode. In the Atlantic, the 20°N–60°N band showed influences of both the combustion mode and the larger hematite dust mode. The Atlantic 70°N–85°N band had a greater influence of the combustion mode. Both the Southern Ocean and the Atlantic 20°S–60°S band had indications of both modes, although low statistics in these regions limited interpretation. Larger-sized dust-like LAM is also evident in the size distribution observed in the Pacific 20°S–20°N region, indicating a greater influence of non-anthropogenic sources to this region[8].

Comparison with global aerosol model predictions

Aircraft ascents and descents from the HIPPO and ATom data sets provided a total of 1187 vertical profiles. These profiles were averaged over four broadly-defined regions over both the Atlantic and Pacific, and one region over the Southern Oceans (colored boxes in Fig. 1) to give a global-scale view of LAM vertical distributions. Figure 6 summarizes the comparison between the average observed LAM vertical profiles (solid black lines), the average vertical profiles for the fraction of LAM aerosols identified as anthropogenic FeO_x-like (solid red lines), and the global modeling results from Matsui et al.[5] for each region (Fig. 6a–i); Fig. 6j shows the ratio between the model predictions and observations for each of the profiles. The model provides monthly climatological average concentrations, and is described in detail in the "Methods" section. The particulate magnetite emissions were estimated in the model[5] as a fixed fraction of BC emissions (not updated here). BC emissions were grouped into anthropogenic (AN) or BB and anthropogenic magnetite emissions were scaled to the AN BC emissions to make the model consistent with the observed FeO_x/rBC mass ratio of 0.4 over East Asia, which had been measured during the A-FORCE campaigns[2]. This emission flux of anthropogenic magnetite was double the anthropogenic iron emission flux in[27].

The model predictions for magnetite mass concentrations were generally lower than the SP2 anthropogenic FeO_x-like observations by a factor of 2–100 (Fig. 6j). The best agreement was in the northern Pacific 20°N–60°N (Fig. 6c) and 60°N–80°N (Fig. 6d), the receptor region for the source area that the model was tuned to. The largest disagreement was over the Southern Oceans, where the model under-predicted magnetite by >10× (Fig. 6i).

As the model generally also under-predicted BC mass loadings by a factor of 1–30 (Supplementary Fig. 16), we show the ratio of observed anthropogenic FeO_x-like to rBC vs. the model

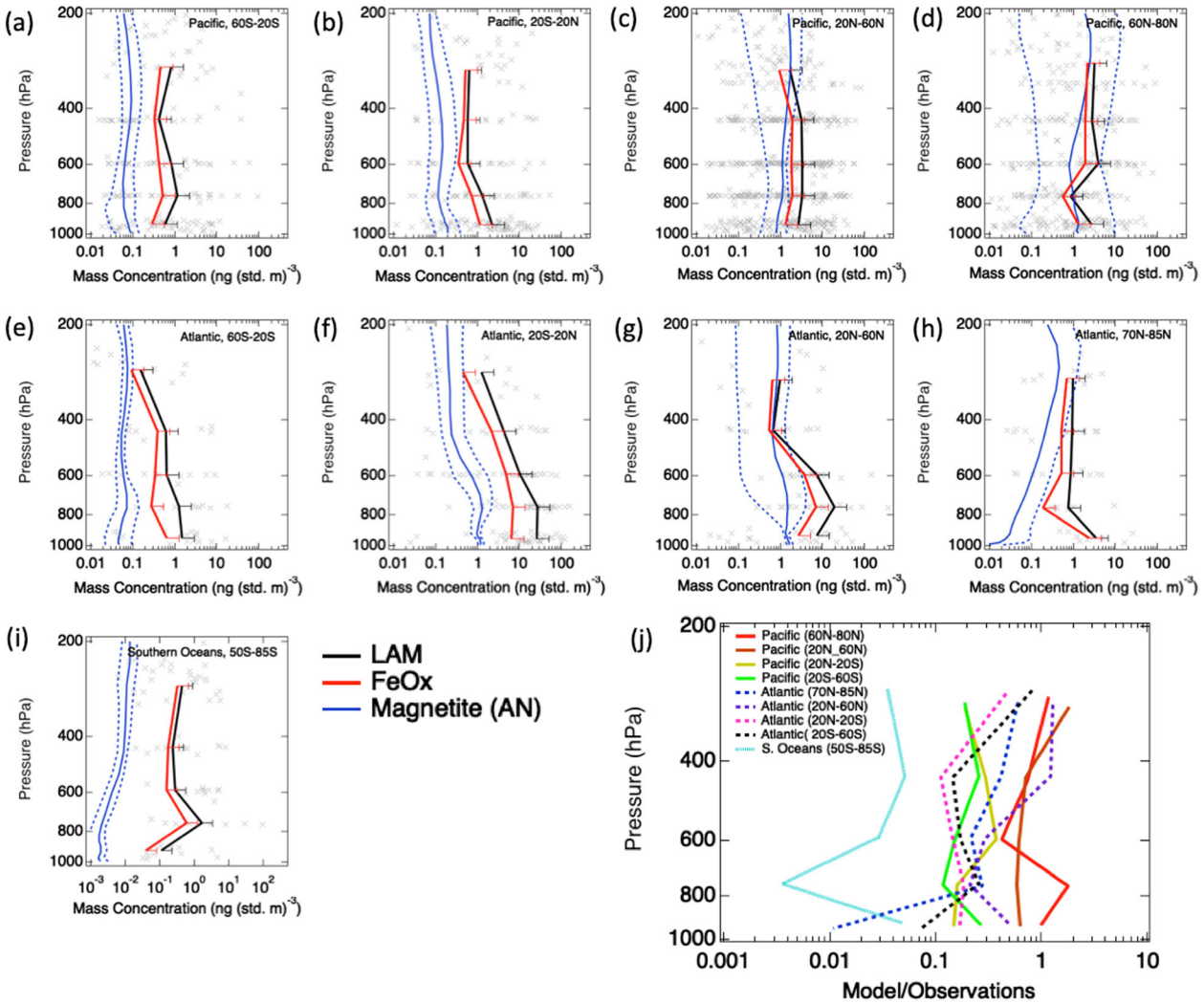

Fig. 6 Comparison of LAM observations to global model estimates of magnetite. Regional average vertical profiles (**a–i**) for the observed LAM (solid black lines) binned to 160 hPa pressure bins, compared with averaged vertical profiles from the CAM5 model for AN (blue) magnetite (solid lines give the annual average, dashed lines are upper and lower ranges for monthly averages for each region). The solid red lines indicate the observed LAM mass associated with FeO_x-like aerosols. Vertical profiles include data from HIPPO 2–5 and ATom 1–4 campaigns. Gray crosses show observations binned for individual vertical sampling periods; bins with zero values are not shown, but are included in the average in each pressure bin for the regional average. The total number of vertical sampling periods included in the average vertical profile for each region are given in parentheses after the region name: *Pacific:* 60°S–20°S (158), 20°S–20°N (159), 20°N–60°N (230), 60°N–80°N (128); *Atlantic:* 60°S–20°S (31), 20°S–20°N (37), 20°N–60°N (34), 70°N–85°N (17); *Southern Ocean* (89). Error bars indicate 1 standard deviation and are only shown for the higher range (assuming observations in a single bin are normally distributed). Note the larger range for the ordinate axis for the vertical profiles over the Southern Ocean. The ratio between the model predictions for AN magnetite and the observed fraction of the LAM mass associated with anthropogenic FeO_x-like aerosols for each region is shown in (**j**).

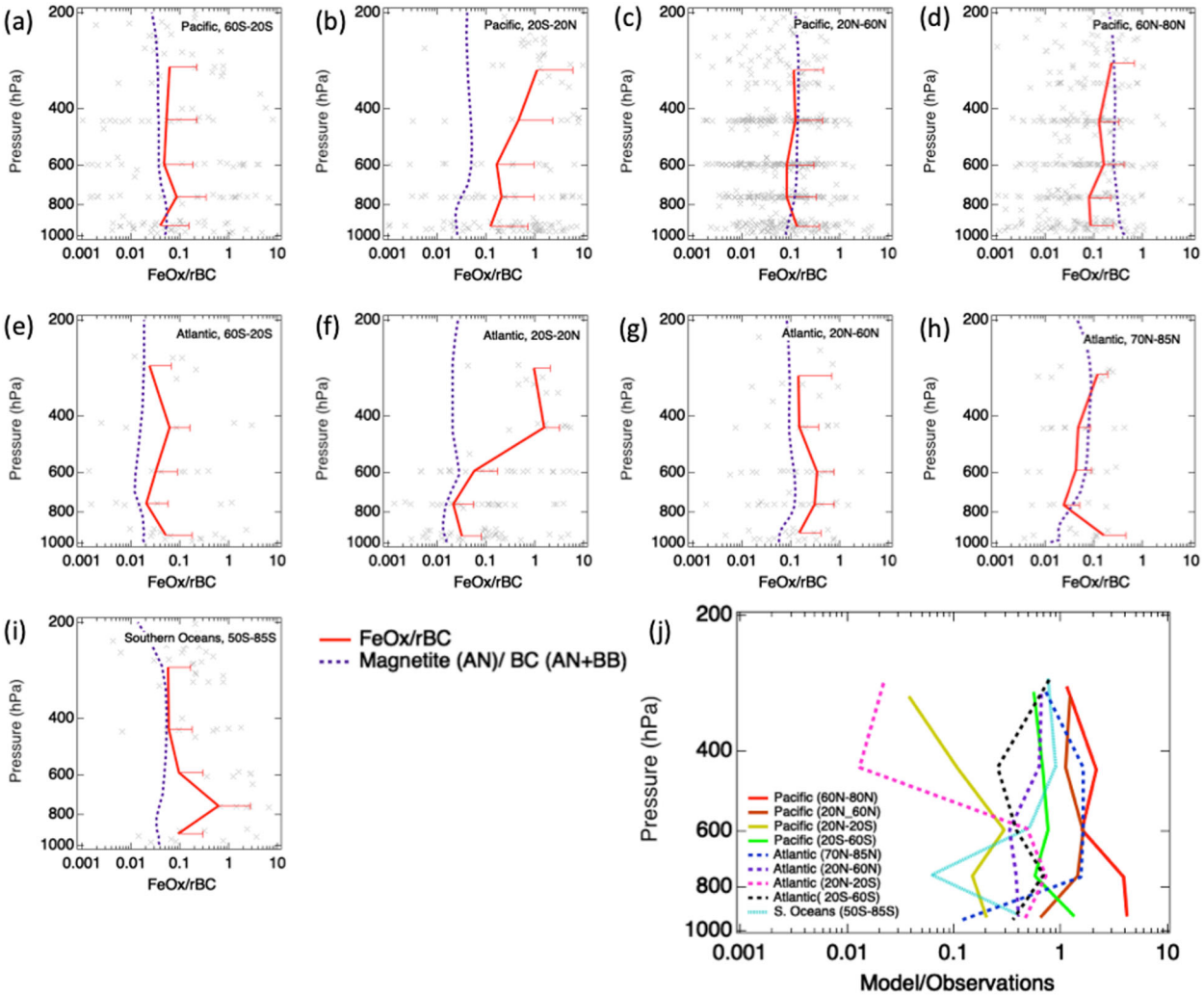

Fig. 7 Comparison of anthropogenic FeO_x/rBC observations to global model estimates of magnetite/BC. Regional average vertical profiles (**a–i**) for the observed anthropogenic FeO_x/rBC (solid red lines) binned to 160 hPa pressure bins, compared with annual averaged vertical profiles from the CAM5 model for AN magnetite/(AN + BB) BC (dashed purple lines). Vertical profiles include data from HIPPO 2–5 and ATom 1-4 campaigns. To determine vertical profiles of the ratio of FeO_x/rBC from observations, average vertical profiles for FeO_x and rBC are calculated for each region (Fig. 6 and Supplementary Fig. 16) and then divided to determine the ratio at each altitude level, as we assume that remote regions are well-mixed. Error bars for the ratio are determined by propagation of uncertainty, under the assumption that errors between observed FeO_x and rBC concentrations are uncorrelated. Gray crosses show observations for the ratio binned during individual vertical sampling periods; bins where FeO_x concentration is 0 are not shown, but are included in the average in each pressure bin for the regional average FeO_x vertical profiles. The ratio between the model predictions and the SP2-observed ratio is shown in (**j**).

predictions for the magnetite to BC ratio for each region in Fig. 7. The model results for the ratio of AN magnetite to the AN + BB BC were compared to the observations, since we assumed the SP2 was sensitive to anthropogenic combustion iron oxides and all BC in the accumulation mode. This comparison provided a better constraint on regional emission ratios of magnetite to BC. While the comparison with the model indicated the observed FeO_x fraction of LAM was higher than the model AN magnetite in most regions (Fig. 6j), the ratio of FeO_x to rBC in every region indicated this discrepancy can mainly be attributed to an underestimation of BC by the model (Fig. 7j). Good agreement between the model ratio and observed ratio was found in most regions in the Atlantic and Pacific (Fig. 7a–i), although the model under-predicted the ratio in the tropics (20°S–20°N), particularly in the Pacific and at altitudes higher than the 600 hPa level (Fig. 7b, f).

The significant under-prediction of FeO_x by the model over the Southern Oceans (Fig. 6i) matched the under-prediction of BC in this region at altitudes higher than 600 hPa (Supplementary Fig. 16i). The FeO_x/rBC ratio binned during individual vertical sampling periods (gray x's in Fig. 7) indicated that while the average ratio at altitudes higher than the 600 hPa level was consistent with the model ratio (Fig. 7i), this was due to averaging over observations with no FeO_x aerosols present and sporadically observed air parcels with relatively high FeO_x/rBC ratios (higher than typical of e.g., the N. Pacific, Fig. 7c), consistent with intermittently enhanced pollution plumes sampled over the Southern Oceans.

Relative shortwave atmospheric heating rates

The relative importance of anthropogenic magnetite towards direct climate effects can be put into context via comparison with BC. The direct radiative effect of absorbing aerosols is a function of both their atmospheric mass loadings and their mass absorption coefficient (MAC). The MAC for FeO_x at the wavelength of 500 nm was previously estimated to be ~2 $m^2 g^{-1}$ for 200 nm diameter particles and 0.6 $m^2 g^{-1}$ for 1 μm particles, ~1/3rd of that of BC[2].

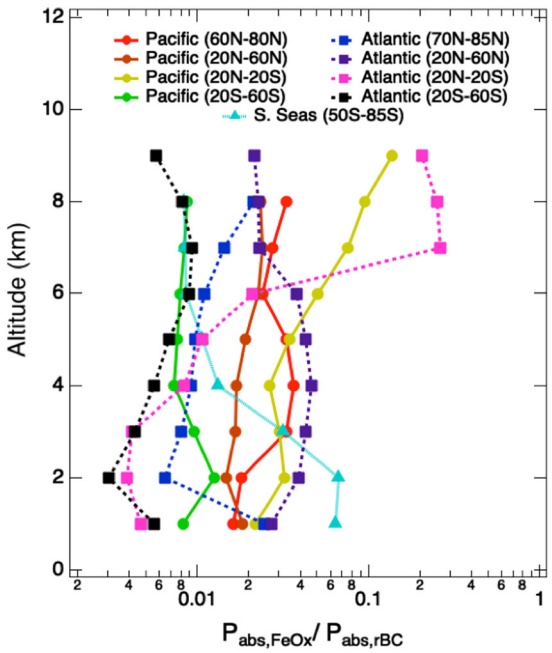

Fig. 8 Relative shortwave atmospheric heating rates. Altitude-dependent instantaneous shortwave atmospheric heating rates (300–2500 nm) for anthropogenic FeO_x-like LAM relative to rBC for each of the regions in cloud-free air. Calculated shortwave heating rates are based on observed mass concentrations and size distributions as well as theoretical calculations for the altitude-dependent actinic flux in each region.

Because the SP2 detected these aerosols via LII, these observations also directly provided evidence that the absorption cross-section of these aerosol particles was significant.

To place a constraint on the direct radiative effects of these aerosols, instantaneous shortwave radiative heating rates were determined from the observed rBC and FeO_x size distributions and mass loadings[2,30] (see "Methods"). Estimated relative shortwave radiative heating rates as a function of altitude for the different regions are shown in Fig. 8. The Pacific had relative shortwave heating rates between 0.7 and 14% compared with rBC, the Atlantic 0.3–26%, and the Southern Ocean 0.8–7%. Previous observations in East Asia found relative shortwave heating rates for FeO_x to rBC in the range of 4–7%[2], although these measurements included ambient FeO_x mass concentrations with diameters up to 2100 nm (see Supplementary Fig. 9 for detection ranges in different campaigns), which was larger than the range we considered here. As previously pointed out in[2], this ratio of relative heating rates for FeO_x relative to rBC was likely a lower limit due to the SP2's inefficient detection of more massive FeO_x particles. Since the detection range of FeO_x by the SP2 in this study only detected ~0.25× the mass range previously observed for FeO_x in East Asia (Supplementary Table 1), assuming a similar mass distribution as previously observed at larger diameters (1290–2100 nm) would increase the relative shortwave heating rates by ~1.7×.

DISCUSSION

Understanding the different aerosol source contributions to direct radiative effects is important for estimating their impact on climate[1]. The ATom and HIPPO observations confirm that FeO_x should be recognized as an anthropogenic contributor to shortwave atmospheric heating rates[2], and indicate their greater importance for radiative effects in the Northern Hemisphere than the Southern Hemisphere (because of the greater influence of anthropogenic combustion sources in these regions). The observations in this study demonstrated that anthropogenic FeO_x-like aerosols were present, at low concentrations, in every region over the remote oceans.

Observed FeO_x concentrations were higher than model predictions from[5] in every region (Fig. 6), even with their higher revised emission estimates for magnetite. This indicates the direct radiative effect of anthropogenic magnetite is higher than that predicted by the model (0.02 W m^{-2} globally)[5]. BC was also underestimated by the model, however, so the relative importance of FeO_x and BC's direct radiative effects are likely broadly consistent with the results in that study. The relative shortwave atmospheric heating rates of FeO_x to rBC on a global scale (0.3–26%) were consistent with the values previously estimated in East Asia in[2]. Since only a portion of FeO_x is observed by the SP2, these observations provide a lower constraint on their total contribution to the global radiative budget.

The similar vertical profiles for both anthropogenic FeO_x (Fig. 6) and rBC (Supplementary Fig. 16) support estimating FeO_x concentrations from combustion sources as a fraction of rBC. Note that that this relationship (Fig. 7j), can vary in different regions and with different sources, and is not a substitute for direct observations. A previous estimate of the atmospheric lifetime of anthropogenic FeO_x relative to rBC (3.2 days vs. 4.5 days)[5] would imply decreasing ratios with increasing transport time from source regions; as particle lifetime is largely controlled by wet removal efficiency, which is expected to be higher for the more massive FeO_x aerosols than for rBC, this is a reasonable expectation. The ratio of magnetite/BC in the model should trend with observed FeO_x/rBC ratio if actual removal rates are similar to those modeled. This is the case in e.g., the Pacific 20°N–60°N region (Fig. 7c) where the model and observations agree within uncertainty. However, our findings are not consistent with this over the large range of transport scales explored. The increasing relative importance of absorption of FeO_x to rBC as a function of altitude in the tropics may be due to differences in aerosol activation and wet scavenging efficiency during convective transport, as has previously been observed for BrC[31–33].

These observations provide additional evidence for more soluble Fe-containing aerosols over the remote oceans associated with anthropogenic combustion sources, as the FeO_x-like aerosols observed by the SP2 had total scattering cross-sections consistent with laboratory samples of pure magnetite and hematite (Supplementary Fig. 6). One challenge of estimating the relative importance of different emission sources for particulate iron deposition to the oceans is that the solubility (which impacts bioavailability) of Fe-containing aerosols is not well-constrained. Iron oxides from combustion sources are believed to have enhanced Fe solubility relative to natural iron oxides due to differences in their chemical and physical properties e.g.,[34–36]. The smaller size mode observed in the dN/dLogD size distributions (Fig. 5a) over the remote oceans also strongly pointed to the presence of anthropogenic combustion iron oxides, even in regions that had significant contributions of mineral dust, such as the SAL over the Atlantic; as the relative Fe solubility of these submicron aerosols is likely significantly higher than dust, they may act as an important contributor to bioavailable Fe for the oceans. Conway et al. recently found better agreement between observed isotopically light Fe in bulk marine aerosols (characteristic of anthropogenic combustion sources) observed over the northern Atlantic and CAM4 model results with a 5× increase in anthropogenic Fe emissions[12]. The regions observed in their isotope-informed simulation for anthropogenic soluble Fe deposition largely coincided with the same regions over the northern Pacific and equatorial Atlantic where we observed significant contributions of anthropogenic FeO_x-like aerosols. Recent isotopic measurements of iron in seawater indicated significant anthropogenic sources from East Asia, with 21–59% of the dissolved Fe

measured in seawater in the N. Pacific (35°N–40°N) attributed to anthropogenic Fe and hence broadly consistent with our observations in this region[13].

Here we have placed constraints on the atmospheric abundance of FeO_x in the Southern Hemisphere. Even the very low concentrations of FeO_x (~0.1 ng (std. m)$^{-3}$) observed over the Southern Ocean in this study could help explain the higher range of aerosol Fe solubility sometimes observed in this region (which cannot be explained by atmospheric processing of mineral dust alone) and the factor of 15 underestimation of soluble Fe concentrations in this region by models[9,37]. The observed average concentrations in this region (Fig. 6i) were at least a factor of 10× higher than predicted in Matsui et al.[5] which already represented 52% higher iron deposition to this region than earlier anthropogenic combustion iron emission estimates would suggest. In this vein, Ito et al. identified a previously unrecognized source of iron to the Southern Oceans—namely Australian bushfires[37]. However, preliminary analysis of very fresh plumes from North American wildfires during the NOAA/NASA FIREX-AQ campaign did not show any significant FeO_x aerosol detectable with the SP2 technique, consistent with a lack of SP2-detected FeO_x enhancements associated with aged Australian fire plumes encountered during ATom. As the model predicted that anthropogenic sources were the major source of FeO_x in this region[5], we infer that the low model bias in this region that we identify on the basis of the SP2 observations would be even more significant in absolute terms when including any possible additional sources from bushfires that cannot be quantified with the SP2. Because of the very low number of particles observed in this region, longer-term monitoring efforts are recommended to provide more robust constraints on FeO_x in this region.

METHODS

Measurements of LAM with a single particle soot photometer

The observations discussed in this study were made using a modified single particle soot photometer (SP2), an instrument that employs laser-induced incandesce to measure and characterize BC-containing aerosols in real time[19]. Measurements were acquired with the NOAA SP2 using 4 detection channels and a 5 MHz acquisition rate. The NOAA SP2 uses a two-element avalanche photodiode as a position-sensitive detector, allowing for estimates of the total scattering cross-section of rBC and LAM aerosols using the leading-edge only fitting method[38]. The detection scheme in the NOAA SP2 is modified from the commercial version to use both a narrow band photomultiplier tube (PMT) with increased sensitivity to red wavelength than standard, and a broad band PMT to detect visible light from incandescing particles[39]; hence we refer to the SP2 used in this study as a modified SP2. The ratio of observed incandescence in the broad and narrow bands is termed the color-temperature ratio, and is proportional to the incandescing particle's blackbody temperature. Aerosols with metallic components that incandesce in the SP2 have lower color-temperature ratios than rBC[21,39,40]. Because the color-temperature ratio depends on the relative alignment of the detectors as well as their gain settings[22] criteria for differentiating LAM signals from rBC signals in the SP2 were determined on a flight-by-flight basis by inspection of the modes in the data for that flight (e.g., Supplementary Fig. 1). Remote aerosols observed in this study showed the highest number densities at color ratios consistent with magnetite and hematite laboratory samples (Supplementary Figs 2, 3). Additional details of the modifications to the NOAA SP2 detection scheme from the typical DMT version can be found in[39,41].

Classification of LAM aerosols

Previous work has demonstrated that laser-induced incandescent (LII) signals from the modified SP2 contain enough information to differentiate between anthropogenic FeO_x particles and mineral dust with metallic oxide components on a single particle basis using optical properties of the particle in addition to their color-temperature ratio[2,21,22]. Because of the low concentrations of LAM observed in remote regions, population-based metrics for classifying aerosols using only a small subset of the total observed particles (such as the one used in[2]) are limited by counting statistics. A supervised machine learning approach can differentiate anthropogenic FeO_x and dust-like FeO_x aerosols on a single particle basis for all aerosols detected by the SP2, but this method is sensitive to instrument calibrations and differences between ambient populations and laboratory samples[22]. Here we use an unsupervised clustering approach to identify three populations of ambient aerosols detected by the SP2 in the metallic mode over both East Asia and over remote regions.

We applied both principle component analysis (PCA) and uniform manifold approximation and projection (UMAP) to single particle SP2 features to identify ambient populations. UMAP is a probabilistic manifold learning technique that can be used to project higher dimensional data into lower dimensions by learning global structures[42], and has recently been applied to physical science data sets as a robust clustering approach (e.g.,[43]). Unlike PCA, UMAP can learn nonlinear relationships between features and is probabilistic (i.e., it learns local structures in higher dimensional data directly from observations).

Both PCA and UMAP-enhanced clustering indicated there were three populations of LAM aerosols in aircraft observations over both South Korea and the remote oceans based on their SP2 LII responses (Supplementary Fig. 4). Based on these populations and comparison with laboratory samples, we established criteria to differentiate anthropogenic FeO_x-like, dust-like, and artifact-like from the incandescent peak height, scattering cross-section at the onset of incandescence, post-incandescent scattering (measurable scattering after the incandescent signal has returned to the baseline), and total scattering cross-section derived from LII signals for single particles (Supplementary Figs 5, 6). Additional details of this classification are found in Supplementary Methods.

The first population of aerosols (anthropogenic FeO_x-like) was identified by higher mass-to-optical-size relationships, more complete evaporation in the beam, and color ratios consistent with laboratory samples of pure iron oxides such as magnetite and hematite. Both scattering cross-section at the onset of incandescence and total scattering cross-section were chosen to be consistent with Mie theory estimates for magnetite (Supplementary Fig. 6).

The second population (dust like) was associated with larger optical sizes (relative to incandescent mass), greater variability in color ratio, and less complete evaporation. Less complete evaporation indicated aerosols were likely internally mixed with materials that do not evaporate in the SP2 laser, rather than pure metallic oxides, as has previously been observed in laboratory samples of mineral dust and coal fly ash[22]. To provide a conservative estimate for anthropogenic FeO_x-like aerosols, any aerosols that fit the optical-size criteria for anthropogenic FeO_x but had significant scattering cross-section after incandescent were classified as dust-like. The SP2 is likely insensitive to a significant fraction of metallic oxides in natural mineral dust due to transport losses in the inlet and sample line, and reduced detection efficiency compared to anthropogenic FeO_x-like particles. The presence of acquired coatings via aging in the atmosphere will not affect classification here[21,23,44].

An additional population of aerosols (artifact-like) associated with in-cloud periods was found in the metallic mode, most prevalently in the HIPPO observations, potentially due to inlet artifacts in ice clouds or highly scattering dust particles (which would both be more prevalent for HIPPO observations due to differences in sampling configuration). These aerosols were generally very large, and on average had lower color-temperature ratios than pure FeO_x, suggesting they predominately consisted of other metallic oxides. As observations are shown for cloud-free regions only (as identified by cloud probes and sampling time scales), only a small fraction of the light-absorbing mass in cloud-free regions was associated with this particle class (1–18% of the mass). We include these particles for completeness in Table 1.

Aircraft observations

In this study we used observations from multiple aircraft campaigns to provide a global picture of atmospheric FeO_x concentrations. Measurements of rBC made with the NOAA SP2 during HIPPO[24,25,45] and during the first ATom campaigns[28,46] have been discussed in detail elsewhere. These measurements have previously been used to constrain the radiative forcing of rBC on a global scale by providing observational constraints on rBC mass loadings in remote regions[28,47,48]. Vertical profiles of rBC mass, mixing state, size distributions and estimated direct radiative effect in East Asia during KORUS-AQ were discussed in[49]. The modified SP2 used in this study observed a smaller size range of FeO_x than that observed in[2]. These factors should be considered when comparing observations between

different aircraft campaigns (Supplementary Fig. 9 and Supplementary Table 1).

Measurements during HIPPO

The HIPPO research campaigns took place in 2009–2011 to measure greenhouse gases and aerosols over the remote Pacific Ocean in 5 distinct seasons[17]. The HIPPO campaigns used the NSF/NCAR GV, sampling at a range of different altitudes (0.3 to 14 km), and latitudes (67°S to 85°N) to provide global coverage over the Pacific far from source regions. Numerous instruments on the airplane monitored atmospheric greenhouse gases (CO, CO_2, H_2O, etc.), cloud droplets, cloud ice, and aerosol parameters[17].

The NOAA SP2 monitored in situ refractory aerosol particles by sampling from a near-isokinetic inlet mounted in a window hatch, with a sampling rate of 4 cm^3 s^{-1}. Before each research flight, the SP2 was calibrated with fullerene soot and 220 nm PSL's to determine laser power. Transmission efficiency of LAM aerosols (assuming a void-free density of 5.17 g cm^{-3} for FeO_x-like particles[2]) sampled on the aircraft from the inlet was >70% for 1.2 µm particles sampled at altitudes below 200 hPa (Supplementary Fig. 8b). Additional aerosol inertial losses inside the NOAA SP2 instrument have previously been investigated inside a pressure chamber, and losses at pressures greater than 200 hPa were <10% for particles with diameters <1 µm[39].

A Cloud Droplet Probe (CDP-2, Droplet Measurement Technology, Longmont CO) was mounted under the left wing of the NSF/NCAR GV, and measured droplets and particles in the range of 2–50 µm. The two-dimensional cloud particle imaging (2D-C) ice probes monitored ice crystals between 25 and 800 µm with the 2D optical array, and ice crystals between 40 and 600 µm with the 1D optical array[50]. Since metallic particles can be generated from ice shattering on the aerosol sampling inlet, strong criteria for removing sampling periods inside clouds have been adopted to avoid contamination by inlet effects. Large dust particles could also potentially lead to similar collisional inlet artifacts. These artifacts can also be enhanced inside liquid water clouds, due to cloud water droplets cleaning off previously deposited particles from the inlet. Therefore, data points (±30 s) where the measured number densities of coarse particles and cloud droplets were greater than 0.1 mL^{-1} (2–50 µm, from CDP-2 measurements) and 0.1 L^{-1} (25–800 µm, 40–600 µm, from 2D-C measurements) have been removed to avoid both ice, dust, and water droplet shattering/cleaning effects. These criteria remove approximately 7% of flight data points. Periods with significant short-term flow fluctuations have also been removed.

SP2 observations from HIPPO 1 could not be used to differentiate LAM from rBC, as the relative alignment of the narrow and broad band PMT detectors did not provide sufficient color-temperature ratio contrast[22]. Data was not available from the HIPPO 2 Antarctic flight (11/11/2009). We also excluded observations from the first two research flights during the HIPPO 4 campaign (06/14/2011 and 06/16/2011), as there were issues with leaks from cabin air that created a large number of spurious particles. These particles differed from the typical aerosols detected in the ambient because of clear temporal patterns.

Measurements during ATom

The ATom research campaigns took place between 2016 and 2018 in four different seasons, sampling over the remote Pacific and remote Atlantic. Numerous instruments monitored aerosols and gases on the NASA DC-8, with measurements of aerosol size distributions from the Aitkens mode to the coarse mode and both bulk and single particle aerosol composition measurements. Typical sampling altitudes were between 0.2 and 11 km.

The NOAA SP2 measured PSL's before each research flight to calibrate laser power. rBC mass was calibrated using fullerene soot laboratory samples size-selected by a differential mobility diameter (DMA) several times during each campaign. During ATom 3 and 4, measurements of Fe_2O_3 and Fe_3O_4 laboratory calibration materials preceding research flights provided further verification of the color-temperature ratio regime for FeO_x. Additional details of SP2 sampling and calibrations during ATom were discussed in detail in[28].

Data from all 4 ATom campaigns were used in this analysis[18]. During these campaigns, the SP2 sampling rate was 4 cm^3 s^{-1}. Periods identified as ice, liquid, or mixed phase clouds were flagged based on the observations from a second generation Cloud, Aerosol, and Precipitation Spectrometer (CAPS)[51]. Additional in-cloud periods were identified by plume length and flagged manually (discussed below). Inlet artifacts are expected to be less significant during ATom than during HIPPO. These criteria removed ~14% of flight data points. ATom 3 Research Flight 11 (10/23/2017) was excluded from the analysis, as one incandescent detector became misaligned shortly after take-off. Transmission efficiency of aerosols sampled on the aircraft from the inlet was >50% for 1.2 µm particles sampled at altitudes below 200 hPa (Supplementary Fig. 8a).

ATom 2 had a higher gain setting for the broad band PMT, which meant that only particles with LAM < 1150 nm were quantified during this campaign. To account for this smaller detection range (180–1150 nm), the FeO_x vertical profile observations from ATom 2 were scaled to match the range of particles detected during other campaigns (180–1290 nm). Based on differences in transmission efficiency and size ranges, a scaling factor of 1.40 was applied to the mass concentration (Supplementary Table 1).

Measurements during KORUS-AQ

The NASA DC8 aircraft flew 20 research flights in and near the South Korean peninsula for 6 weeks in May-June of 2016, sampling between 0.3 and 7.5 km over land and 0.15 and 7.5 km over the ocean. SP2 observations of rBC during KORUS-AQ have been discussed in detail in[49]. During KORUS-AQ, two SP2's were flown on the NASA DC-8, one sampling after a dryer and another with a humidification system maintained at 80% RH. As the alignment of the incandescent detectors in the dry SP2 prevented the color ratio from being accurately measured, we instead used observations from the humidified SP2, which was available for 17 of 20 research flights. The SP2 was not operational during 2 flights (05/12/2016 and 05/16/2016). Due to in-flight leaks of cabin air, 2/3rds of another flight was not usable (05/19/2016). The humidification may impact the initial optical size of the aerosols (due to hygroscopic growth), but does not impact the color ratio or incandescent peak height measured by the SP2[52]. Sampling flow rates for the SP2's during KORUS-AQ were 2 cm^3 s^{-1}. In-cloud periods and periods with significant fluctuations in sampling pressure have also been removed as discussed in[49].

Spatial scale requirement

An additional criterion was applied to all the data sets to eliminate spurious impacts of shattering events for the remote observations. Since previous analysis[53] has indicated that the typical rBC plumes in remote regions observed during the HIPPO campaigns were between 34 and 648 km, we assumed any significant increases in concentration of LAM above the background at smaller spatial scales than the minimum plume length were likely associated with inlet shattering events. These events were identified based on their 10 s average number density, with values greater than 1.0 (std. m)$^{-3}$ flagged and removed. This value was chosen as it represented an outlier relative to all observations during ATom and HIPPO.

Sampling statistics

We performed a Monte Carlo simulation (similar to the one in[24]) to determine the sampling volume needed to eliminate the effects of counting statistics on the observed LAM concentrations. This relationship is shown in Supplementary Fig. 11. For 1 ng (std. m)$^{-3}$, approximately 10 min of aircraft sampling at 4 cm^3 s^{-1} were required to reach statistical significance, with longer averaging times required for lower concentrations or at high altitudes. We identify a "strong sampling criterion" as providing at worst 50% statistical uncertainty on the concentration, and a "weak sampling criterion" as sufficient integration to allow detection of at least one LAM. This motivated our choice to bin data broadly to 0.5 km and 1.0° latitude for reporting the LAM mass mixing ratio and generally limited reporting LAM concentrations to broadly-defined latitude bands, in order to provide sufficient sampling time in remote regions. We assume that observations in remote regions are well-mixed. Additional details are provided in Supplementary Methods, which also assess the constraints on possible LAM concentration provided by cases in which no LAM was detected. Sampling over the Atlantic in the ATom dataset accounted for only about 1/3rd of the sampling time compared with the Pacific during both ATom and HIPPO (2600 L vs. 7100 L, Supplementary Table 2).

Estimation of shortwave atmospheric heating rates

Following the approach in[2,30], we estimated the shortwave atmospheric heating rates for FeO_x relative to rBC to provide a constraint on anthropogenic magnetite radiative effects in different regions. To estimate actinic flux for wavelengths between 300 and 2500 nm from the surface up

to 12 km in cloud-free air, the libRadtran software package (v. 2.0.2) was used[54,55]. We used the size-resolved MAC values for BC and magnetite as determined by a discrete-dipole approximation calculation in[2], who used indices of refraction for magnetite measured between 300 and 2400 nm[56]. We assumed aerosols have a single scattering albedo of 0.85 and an asymmetry parameter of 0.7, with b_{ext} calculated based on our observed dM/dLogD size distributions for rBC and FeO_x following[2]. The solar zenith angle for each region was determined at local noon on the fall equinox at the central latitude and longitude location for that region. An albedo of 0.2 was assumed for the surface. The radiative transfer equation solver sdisort was used with 6 streams and the LOWTRAN molecular absorption parameterization was used for gas phase absorption. Atmospheric vertical profiles of gases used default values for mid-latitude summer (60°S to 20°S and 60°N to 20°N), tropical (20°S to 20°N), and sub-arctic summer (60°N to 80°N and the Southern Ocean).

Global aerosol model

Modeling results are from CAM5-chem/ATRAS2[57,58]. In this model, anthropogenic magnetite is considered explicitly, and simulated magnetite/BC ratios were constrained with the observed values in East Asia during the A-FORCE campaign[5]. A power law function size distribution of FeO_x observed during the A-FORCE campaign was used in the model and assumed no emissions of magnetite particles >3 µm in diameter. Since the SP2 used in this study only measures FeO_x aerosols in the range of 180–1290 nm volume equivalent diameter (assuming a void-free density of 5.17 g cm^{-3}), we compare only with the modeled magnetite in the size bins between 230 and 1250 nm diameter. BC concentrations are reported for shell + core dry diameters between 90-1250 nm. All aerosol species were assumed to be internally mixed. Model results, available on a monthly average basis, were not generated for the specific years when the measurements were performed, but rather based on climatological averages over 5 years (after a 1 year spin-up period). Comparison to FeO_x observations were based on averaging over the time periods most consistent with the timing for the ATom and HIPPO flight campaigns. HIPPO 2 included data from October to November; HIPPO 3, March to April; HIPPO 4, June to July; HIPPO 5, August to September; ATom 1, August; ATom 2, February; ATom 3, October; ATom 4, April to May. Comparison of model results with the observations of rBC during HIPPO 1 were discussed in[58]. Simulated BC concentrations may be underestimated at high latitudes because all model BC was assumed to be internally mixed in[5]. Additionally, BC emissions in the model results came from the CMIP5 emission data for the year 2000, which may underestimate emissions for the more recent HIPPO and ATom campaigns. The model does not include secondary aerosol activation and removal processes above cloud base, which may lead to overpredictions of aerosol loadings in the middle and upper troposphere[59].

DATA AVAILABILITY

HIPPO campaign data can be found at https://esrl.noaa.gov/csl/groups/csl6/measurements/. https://data.eol.ucar.edu/dataset/117.102—HIPPO-2
https://data.eol.ucar.edu/dataset/121.024—HIPPO-3
https://data.eol.ucar.edu/dataset/248.025—HIPPO-4
https://data.eol.ucar.edu/dataset/249.024—HIPPO-5
ATom campaign data can be found at https://espoarchive.nasa.gov/archive/browse/ATom. KORUS-AQ campaign data can be found at https://www-air.larc.nasa.gov/cgi-bin/ArcView/korusaq.

CODE AVAILABILITY

Code developed for the analysis of the SP2 observations is available upon request from the authors. The libRadTran software package is available at http://www.libradtran.org/doku.php. Code for the UMAP algorithm is available at https://umap-learn.readthedocs.io/en/latest/.

Received: 20 July 2020; Accepted: 12 February 2021;
Published online: 12 March 2021

REFERENCES

1. Samset, B. H. et al. Aerosol absorption: progress towards global and regional constraints. *Curr. Clim. Change Rep.* **4**, 65–83 (2018).
2. Moteki, N. et al. Anthropogenic iron oxide aerosols enhance atmospheric heating. *Nat. Commun.* **8**, 1–11 (2017).
3. Yoshida, A. et al. Abundance and emission flux of the anthropogenic iron oxide aerosols from the East Asian continental outflow. *J. Geophys. Res. Atmos.* **123**, 11–194 (2018).
4. Ohata, S. et al. Abundance of light-absorbing anthropogenic iron oxide aerosols in the urban atmosphere and their emission sources. *J. Geophys. Res. Atmos.* **123**, 8115–8134 (2018).
5. Matsui, H. et al. Anthropogenic combustion iron as a complex climate forcer. *Nat. Commun.* **9**, 1593 (2018).
6. Ito, A., Lin, G. & Penner, J. E. Radiative forcing by light-absorbing aerosols of pyrogenetic iron oxides. *Sci. Rep.* **8**, 7347 (2018).
7. Scanza, R. A. et al. Atmospheric processing of iron in mineral and combustion aerosols: development of an intermediate-complexity mechanism suitable for Earth system models. *Atmos. Chem. Phys.* **18**, 14175–14196 (2018).
8. Mahowald, N. M. et al. Aerosol trace metal leaching and impacts on marine microorganisms. *Nat. Commun.* **9**, 2614 (2018).
9. Ito, A. et al. Pyrogenic iron: the missing link to high iron solubility in aerosols. *Sci. Adv.* **5**, eaau7671 (2019).
10. Meskhidze, N. et al. Perspective on identifying and characterizing the processes controlling iron speciation and residence time at the atmosphere-ocean interface. *Mar. Chem.* **217**, 103704 (2019).
11. Kurisu, M. et al. Variation of iron isotope ratios in anthropogenic materials emitted through combustion processes. *Chem. Lett.* **45**, 970–972 (2016).
12. Conway, T. M. et al. Tracing and constraining anthropogenic aerosol iron fluxes to the North Atlantic Ocean using iron isotopes. *Nat. Commun.* **10**, 2628–2628 (2019).
13. Pinedo-González, P. et al. Anthropogenic Asian aerosols provide Fe to the North Pacific Ocean. *Proc. Natl Acad. Sci. U.S.A.* **117**, 27862–27868 (2020).
14. Ito, A. & Shi, Z. Delivery of anthropogenic bioavailable iron from mineral dust and combustion aerosols to the ocean. *Atmos. Chem. Phys.* **16**, 85–99 (2016).
15. Kurisu, M., Takahashi, Y., Iizuka, T. & Uematsu, M. Very low isotope ratio of iron in fine aerosols related to its contribution to the surface ocean. *J. Geophys. Res. Atmos.* **121**, 11–119 (2016).
16. Li, W. et al. Air pollution–aerosol interactions produce more bioavailable iron for ocean ecosystems. *Sci. Adv.* **3**, e1601749 (2017).
17. Wofsy, S. C. HIAPER Pole-to-Pole Observations (HIPPO): fine-grained, global-scale measurements of climatically important atmospheric gases and aerosols. *Philos. Trans. R. Soc. Lond. Ser. A* **369**, 2073–2086 (2011).
18. Wofsy, S. C. & ATom Science Team. ATom: aircraft flight track and navigational data. ORNL DAAC. https://doi.org/10.3334/ORNLDAAC/1613 (2018).
19. Stephens, M., Turner, N. & Sandberg, J. Particle identification by laser-induced incandescence in a solid-state laser cavity. *Appl. Opt.* **42**, 3726–3736 (2003).
20. Lack, D. A., Moosmüller, H., McMeeking, G. R., Chakrabarty, R. K. & Baumgardner, D. Characterizing elemental, equivalent black, and refractory black carbon aerosol particles: a review of techniques, their limitations and uncertainties. *Anal. Bioanal. Chem.* **406**, 99–122 (2014).
21. Yoshida, A. et al. Detection of light-absorbing iron oxide particles using a modified single-particle soot photometer. *Aerosol Sci. Technol.* **50**, 1–4 (2016).
22. Lamb, K. D. Classification of iron oxide aerosols by a single particle soot photometer using supervised machine learning. *Atmos. Meas. Tech.* **12**, 3885–3906 (2019).
23. Yoshida, A. et al. Abundances and microphysical properties of light-absorbing iron oxide and black carbon aerosols over East Asia and the Arctic. *J. Geophys. Res.: Atmos.* **125**, e2019JD032301 (2020).
24. Schwarz, J. P. et al. Global-scale seasonally resolved black carbon vertical profiles over the Pacific. *Geophys. Res. Lett.* **40**, 5542–5547 (2013).
25. Schwarz, J. P. et al. Aircraft measurements of black carbon vertical profiles show upper tropospheric variability and stability. *Geophys. Res. Lett.* **44**, 1132–1140 (2017).
26. Shen, Z. et al. Analysis of transpacific transport of black carbon during HIPPO-3: implications for black carbon aging. *Atmos. Chem. Phys.* **14**, 6315–6327 (2014).
27. Luo, C. et al. Combustion iron distribution and deposition. *Global Biogeochem. Cycles*. **22,** 1–17 (2008).
28. Katich, J. M. et al. Strong contrast in remote black carbon aerosol loadings between the Atlantic and Pacific basins. *J. Geophys. Res. Atmos.* **123**, 13–386 (2018).
29. Liu, D. et al. Aircraft and ground measurements of dust aerosols over the west African coast in summer 2015 during ICE-D and AER-D. *Atmos. Chem. Phys.* **18**, 3817–3838 (2018).
30. Gao, R. S. et al. Calculations of solar shortwave heating rates due to black carbon and ozone absorption using in situ measurements. *J. Geophys. Res. Atmos*. **113,** 1–11 (2008).
31. Zhang, Y. et al. Top-of-atmosphere radiative forcing affected by brown carbon in the upper troposphere. *Nat. Geosci.* **10**, 486–489 (2017).

32. Zhang, A. et al. Modeling the global radiative effect of brown carbon: a potentially larger heating source in the tropical free troposphere than black carbon. *Atmos. Chem. Phys.* **20**, 1901–1920 (2020).
33. Zeng, L. et al. Global measurements of brown carbon and estimated direct radiative effects. *Geophys. Res. Lett.* **47**, e2020GL088747 (2020).
34. Sedwick, P. N., Sholkovitz, E. R. & Church, T. M. Impact of anthropogenic combustion emissions on the fractional solubility of aerosol iron: Evidence from the Sargasso Sea. *Geochem. Geophys. Geosyst.* **8,** 1–21 (2007).
35. Srinivas, B., Sarin, M. M. & Kumar, A. Impact of anthropogenic sources on aerosol iron solubility over the Bay of Bengal and the Arabian Sea. *Biogeochemistry* **110**, 257–268 (2012).
36. Ito, A. Atmospheric processing of combustion aerosols as a source of bioavailable iron. *Environ. Sci. Technol. Lett.* **2**, 70–75 (2015).
37. Ito, A. et al. Evaluation of aerosol iron solubility over Australian coastal regions based on inverse modeling: implications of bushfires on bio-accessible iron concentrations in the Southern Hemisphere. *Prog. Earth Planet Sci.* **7**, 42 (2020).
38. Gao, R. S. et al. A novel method for estimating light-scattering properties of soot aerosols using a modified single-particle soot photometer. *Aerosol Sci. Technol.* **41**, 125–135 (2007).
39. Schwarz, J. P. et al. Single-particle measurements of mid-latitude black carbon and light-scattering aerosols from the boundary layer to the lower stratosphere. *J. Geophys. Res. Atmos.* **111**, 1–15 (2006).
40. Moteki, N. & Kondo, Y. Dependence of laser-induced incandescence on physical properties of black carbon aerosols: Measurements and theoretical interpretation. *Aerosol Sci. Technol.* **44**, 663–675 (2010).
41. Schwarz, J. P. et al. The detection efficiency of the single particle soot photometer. *Aerosol Sci. Technol.* **44**, 612–628 (2010).
42. McInnes, L., Healy, J. & Melville, J. UMAP: Uniform manifold approximation and projection for dimension reduction. Preprint at https://arxiv.org/abs/1802.03426 (2018).
43. Becht, E. et al. Dimensionality reduction for visualizing single-cell data using UMAP. *Nat. Biotechnol.* **37**, 38–44 (2019).
44. Moteki, N. & Kondo, Y. Effects of mixing state on black carbon measurements by laser-induced incandescence. *Aerosol Sci. Technol.* **41**, 398–417 (2007).
45. Schwarz, J. P. et al. Global-scale black carbon profiles observed in the remote atmosphere and compared to models. *Geophys. Res. Lett.* **37**, 1–5 (2010).
46. Lund, M. et al. Short Black Carbon lifetime inferred from a global set of aircraft observations. *npj Clim. Atmos. Sci.* **1**, 1–8 (2018).
47. Wang, Q. et al. Global budget and radiative forcing of black carbon aerosol: Constraints from pole-to-pole (HIPPO) observations across the Pacific. *J. Geophys. Res. Atmos.* **119**, 195–206 (2014).
48. Samset, B. H. et al. Modelled black carbon radiative forcing and atmospheric lifetime in AeroCom Phase II constrained by aircraft observations. *Atmos. Chem. Phys.* **14**, 12465–12477 (2014).
49. Lamb, K. D. et al. Estimating source region influences on black carbon abundance, microphysics, and radiative effect observed over South Korea. *J. Geophys. Res. Atmos.* **123**, 13–527 (2018).
50. Korolev, A. V. et al. Small ice particles in tropospheric clouds: fact or artifact? airborne icing instrumentation evaluation experiment. *Bull. Am. Meteorol. Soc.* **92**, 967–973 (2011).
51. Spanu, A., Dollner, M., Gasteiger, J., Bui, T. P. & Weinzierl, B. Flow-induced errors in airborne in situ measurements of aerosols and clouds. *Atmos. Meas. Tech.* **13** 1963–1987 (2020).
52. Schwarz, J. P. et al. Technique and theoretical approach for quantifying the hygroscopicity of black-carbon-containing aerosol using a single particle soot photometer. *J. Aerosol Sci.* **81**, 110–126 (2015).
53. Weigum, N. M., Stier, P., Schwarz, J. P., Fahey, D. W. & Spackman, J. R. Scales of variability of black carbon plumes over the Pacific Ocean. *Geophys. Res. Lett.* **39**, 1–5 (2012).
54. Mayer, B. & Kylling, A. The libRadtran software package for radiative transfer calculations-description and examples of use. *Atmos. Chem. Phys.* **5**, 1855–1877 (2005).
55. Emde, C. et al. The libRadtran software package for radiative transfer calculations (version 2.0. 1). *Geosci. Model Dev.* **5**, 1647–1672 (2016).
56. Huffman, D. R. & Stapp, J. L. *Interstellar Dust and Related Topics: IAU Symposium No. 52.* Greenberg, J. M. & H. C. Van De Hulst, eds. Reidel, Boston (1973), 297–301 (1973).
57. Matsui, H. Development of a global aerosol model using a two-dimensional sectional method: 1. Model design. *J. Adv. Model. Earth Syst.* **9**, 1921–1947 (2017).
58. Matsui, H. & Mahowald, N. Development of a global aerosol model using a two-dimensional sectional method: 2. Evaluation and sensitivity simulations. *J. Adv. Model. Earth Syst.* **9**, 1887–1920 (2017).
59. Yu, P. et al. Efficient in-cloud removal of aerosols by deep convection. *Geophys. Res. Lett.* **46**, 1061–1069 (2019).

ACKNOWLEDGEMENTS

We thank Dr. Nobuhiro Moteki for providing the MAC calculations for rBC and FeO_x from ref. [2]. We thank Dr. RuShan Gao and Dr. David Fahey for their contributions to NOAA SP2 observations during the HIPPO campaigns. Melanie Thatcher is acknowledged for her contribution to the laboratory measurements. The Langley Aerosol Research Group is acknowledged for providing the cloud cuts during KORUS-AQ, and the NCAR/EOL Particle Measuring Systems Group for providing the cloud probe data during HIPPO; we would also like to acknowledge the contributions of all the pilots, crew, and supporting scientists during the ATOM, HIPPO, and KORUS-AQ campaigns. The NOAA SP2 data were obtained and analyzed with the support of the NASA Radiation Sciences Program, the NASA Upper Atmosphere Research Program, and the NOAA Atmospheric Composition and Climate Program. H.M. was supported by the Ministry of Education, Culture, Sports, Science, and Technology and the Japan Society for the Promotion of Science (MEXT/JSPS) KAKENHI Grant Numbers JP17H04709, JP16H01770, JP19H04253, JP19H05699, JP19KK0265, and JP20H00638, by the MEXT Arctic Challenge for Sustainability (ArCS) and ArCS-II projects, and by the Environment Research and Technology Development Fund (2-1703 and 2-2003) of the Environmental Restoration and Conservation Agency. B.W. and M.D. have received funding from the European Research Council (ERC) under the European Union's Horizon 2020 Research and Innovation Framework Program under grant No. 640458 (A-LIFE).

AUTHOR CONTRIBUTIONS

K.D.L. conceived the idea, led the FeO_x analysis for the NOAA SP2, and wrote the paper, with guidance from J.P.S. H.M. adapted the emission scheme and performed the modeling in CAM5. J.M.K. and J.P.S. acquired the SP2 observations during the ATom campaigns. B.W. and M.D. acquired the CAPS aerosol and cloud probe observations during ATom and derived times of cloud passages and cloud phase. J.M.K. analyzed the rBC observations during ATom. A.E.P., J.R.S., and J.P.S. acquired the SP2 observations and performed the rBC analysis during the HIPPO campaigns. K.D.L., A.E.P., and J.P.S. acquired the SP2 measurements during the KORUS-AQ campaigns, and K.D.L. led the rBC analysis for the SP2 during KORUS-AQ. K.D.L. performed the laboratory measurements, the Monte Carlo simulations, and the estimation of shortwave heating rates.

COMPETING INTERESTS

The authors declare no competing interests.

ADDITIONAL INFORMATION

Supplementary information The online version contains supplementary material available at https://doi.org/10.1038/s41612-021-00171-0.

Correspondence and requests for materials should be addressed to K.D.L.

Reprints and permission information is available at http://www.nature.com/reprints

Publisher's note Springer Nature remains neutral with regard to jurisdictional claims in published maps and institutional affiliations.